

FULL PAPER

Open Access



Utility of Slepian basis functions for modeling near-surface and satellite magnetic anomalies of the Australian lithosphere

Hyung Rae Kim^{1*}  and Ralph R. B. von Frese²

Abstract

The utility of frequency- and space-limited spherical harmonic Slepian basis functions for magnetic anomaly modeling over restricted spherical patches of the Earth was investigated using combined near-surface scalar and CHAMP satellite vector observations from Australia and adjacent marine areas. In particular, Slepian spherical harmonic models up to degree 360 were studied for modeling anomaly features of 1° (~111 km) and longer over a 25°-radius cap centered on Australia. Relative to the roughly 130,000 coefficients required for global spherical harmonic modeling, less than 5% of this number of coefficients is sufficient for effective localized Slepian modeling. Slepian coefficients have maximum power over the spherical cap and may be exploited for estimating the magnetic anomaly vectors and gradients to all orders within the working precision of the observations. The Earth cap modeled by Slepian coefficients is also more efficient in accommodating local crustal constraints from drilling and other geological and geophysical studies for interpreting the associated magnetic anomaly data registered in spherical coordinates. In general, Slepian spherical harmonic modeling is well suited for combining spectrally diverse compilations of near-surface and satellite magnetic observations over any spatially restricted spherical cap of the Earth or other planetary body.

Keywords: Spherical Slepian harmonics, Australia, Magnetic anomalies, CHAMP, Joint inversion, ADMAP-2

Introduction

The confirmation of lithospheric components in low Earth orbiting satellite magnetic observations spawned numerous investigations showing the enhanced interpretational utility of combined satellite and near-surface magnetic anomaly data (e.g., Hildenbrand et al. 1996; Langel and Hinze 1998; von Frese et al. 1999; Ravat et al. 2002; Kim et al. 2004; Hinze et al. 2013). In general, the combined anomaly data provide significant insights on the geologic, tectonic, and thermal processes of the lithosphere, as well as on crustal resources and natural hazards at local and regional scales (e.g., Blakely 1995; Hinze et al. 2013).

Conventional spherical harmonic modeling needs full data coverage of the Earth that only satellite observations may provide with a relatively uniform error budget. Satellite observations essentially recover longer-wavelength anomaly features, but not the higher-frequency anomalies near the Earth's surface due to the measurement errors (e.g., Kim et al. 2004; von Frese et al. 2005). Thus, the shorter-wavelength near-surface anomalies from terrestrial, shipborne, and airborne magnetic surveys provide important constraints to augment lithospheric studies of the satellite magnetic data. The near-surface data, on the other hand, also commonly suffer from corrupted longer-wavelength components due to measurement errors and non-uniform survey coverage so that satellite observations also yield important regional anomaly constraints for lithospheric analysis.

As an example, consider the global spherical harmonic model (NGDC720) of magnetic anomalies of the

*Correspondence: kimhr@kongju.ac.kr

¹ Department of GeoEnvironmental Science, Kongju National University, Gongju, Chungnam, South Korea

Full list of author information is available at the end of the article

lithosphere up to degree 720 that Maus (2010) produced from the 2-arc-min (~ 5 km)-resolution Earth magnetic anomaly grid (EMAG2). The EMAG2 grid, in turn, was compiled from available near-surface magnetic surveys with large coverage gaps that were augmented with anomaly values based on an oceanic crustal age model and satellite magnetic observations (Maus et al. 2009). The global spherical harmonic NGDC720 model required massive computing to evaluate the 518,399 coefficients to represent the EMAG2 anomaly wavelengths down to ~ 56 km at the equator (Maus 2010). Clearly, updating the NGDC720 model for gap filling and other new data poses significant computational challenges. Slepian spherical harmonic modeling, by contrast, offers a computationally efficient alternative for representing the survey data to the maximum degree permitted by the data interval and available computing capacity.

To investigate these computational efficiencies, the present study implements the Slepian modeling of spherically registered near-surface and satellite magnetic anomalies in the 25° -radius cap centered on Australia to a degree 360 resolution. To accommodate this application, roughly 130,000 global spherical harmonic coefficients are required relative to Slepian modeling that needs only about 6104 coefficients, and thus offers significant computational advantages for updating the near-surface and satellite data.

Additional approaches to local spherical coordinate magnetic anomaly analyses have invoked inversions using equivalent point dipoles (e.g., von Frese 1998; von Frese et al. 1981, 1988; Hinze et al. 2013) and spherical cap harmonic functions (e.g., Haines 1985, 1990; Thébault et al. 2006). Spherical cap harmonic functions in particular have been widely applied for modeling main field and secular variations (e.g., Haines 1985; Kotzé 2001; Gaya-Piqué et al. 2006), and lower-order lithospheric components of the Earth's magnetic field (Coles 1985; de Santis et al. 1989; Kovács et al. 2011). Lesur (2006) also introduced a 'quasi-local' function of band-limited wavelets to model the main geomagnetic field of any subregion of the globe.

The Slepian method also has been used to evaluate the continental and oceanic power spectrum components from the global spherical harmonic coefficients of the geomagnetic field (Beggan et al. 2013), and for modeling south polar Martian magnetic anomalies from the Mars Global Surveyor satellite data (Plattner and Simons 2015). These Slepian-based studies, however, were restricted to single-altitude grids of satellite-based observations.

Joint inversion efforts to combine near-surface and satellite magnetic observations, on the other hand, have used spherical point dipole or prism models to study how the anomalies may transition from near-surface to

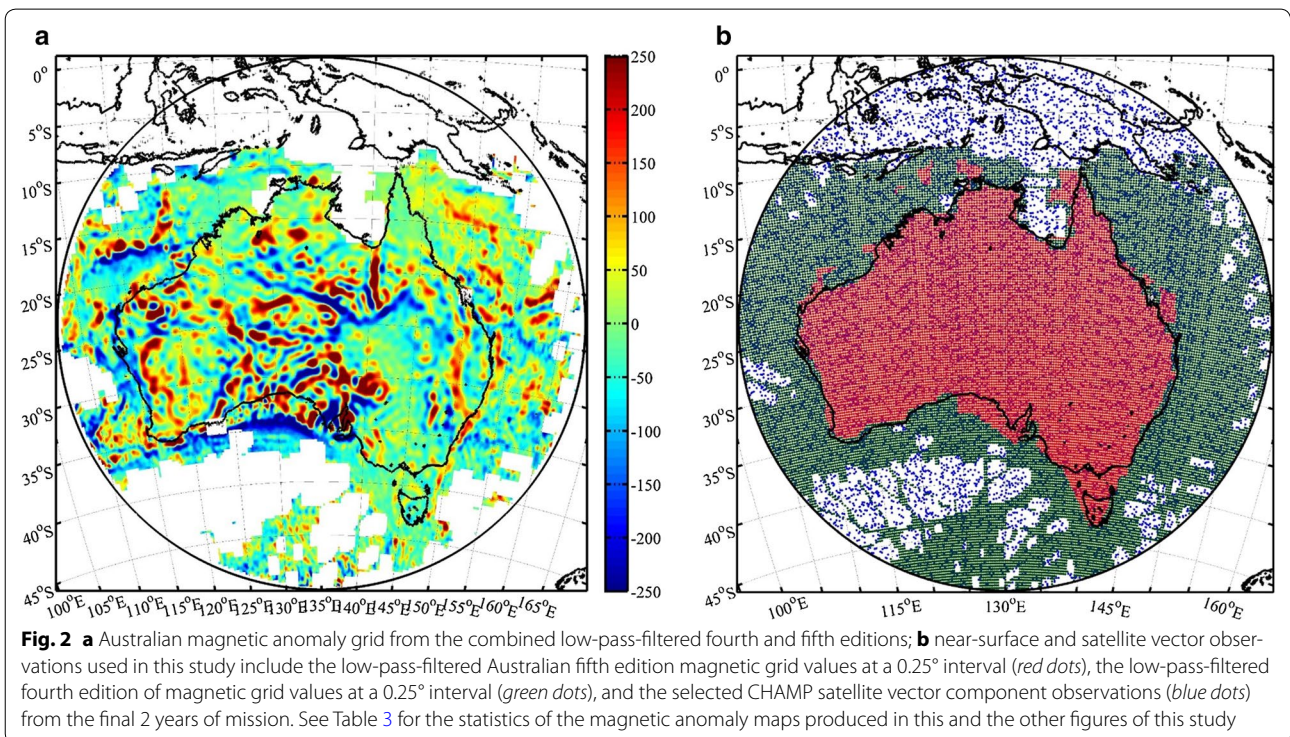
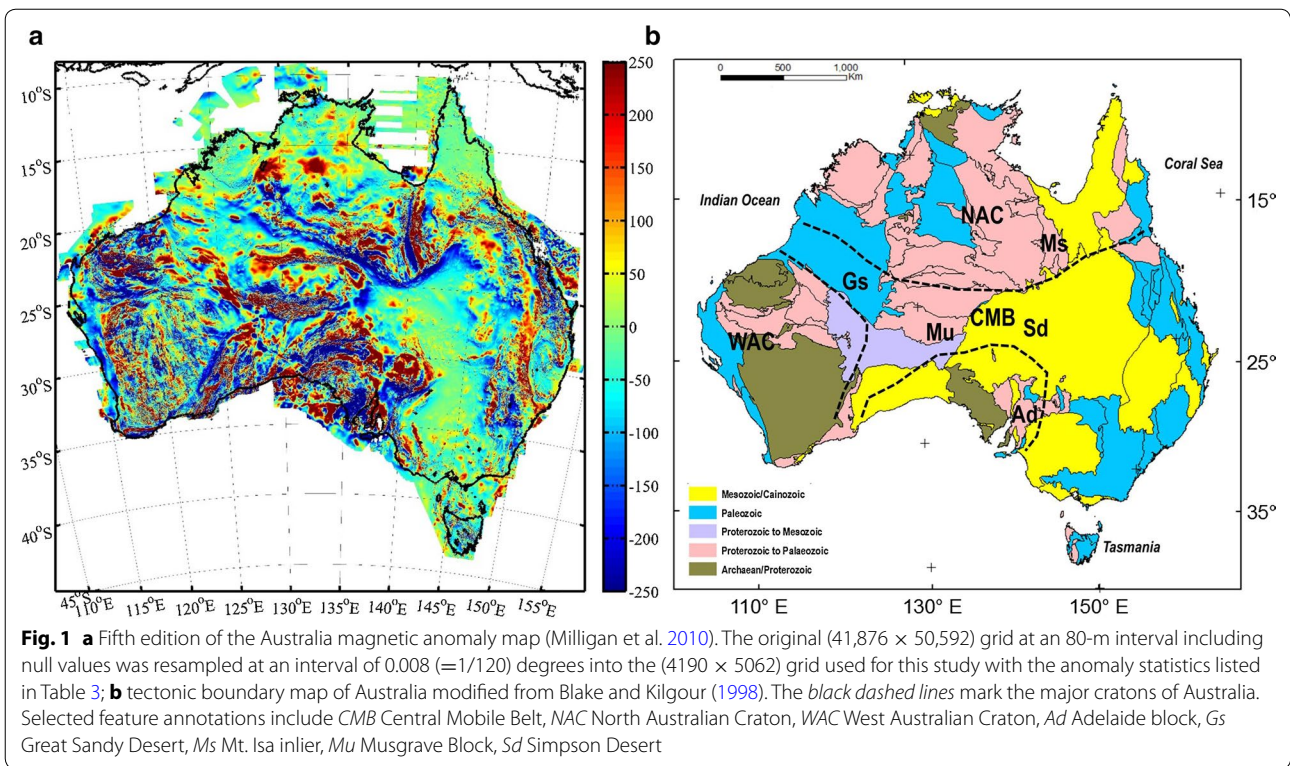
satellite altitudes (e.g., von Frese et al. 1999; Ravat et al. 2002; Milligan et al. 2004; Kim et al. 2004, 2005, 2007). In the present study, spherical Slepian functions are developed for fitting both near-surface scalar and satellite vector observations over Australia to study the altitude behavior of the anomalies.

Data

Basic data on the near-surface anomalies were obtained from both the Australian fourth and fifth edition total intensity magnetic anomaly grids (Milligan and Franklin 2004; Milligan et al. 2010). Figure 1a shows the fifth edition grid for the Australian mainland and Tasmania and restricted offshore areas. It was updated from the fourth edition grid that provided additional coverage into the Indian Ocean on the west and the Coral Sea to the east. To make the inversions more computationally tractable for this study, both grids were low-pass-filtered for roughly 1° and longer (≥ 111 km)-wavelength anomalies and resampled at a 0.25° (~ 27 km) interval. The Australian mainland and Tasmania were populated with anomaly values from the fifth edition grid, whereas the other areas were populated from the fourth edition grid and CHAMP satellite data as shown in Fig. 2.

Satellite vector component anomaly data from the CHAMP mission were downloaded from the National Space Institute of the Technical University of Denmark (DTU, http://www.space.dtu.dk/english/Research/Scientific_data_and_models/Magnetic_Field_Models). These observations selected from the final 2 years of the lower-altitude CHAMP mission data were used to produce the main and lithospheric field components of the CHAOS—4h model (Olsen et al. 2014). The core and external field components from the CHAOS—4h model, were subtracted from these CHAMP observations to obtain residuals presumably dominated by lithospheric components. To further facilitate the computations of this demonstration, the residual anomalies were down-sampled by rejecting values outside of one standard deviation of the lithospheric anomaly predictions from the CHAOS—4h model. Accordingly, a total of 13,568 residual CHAMP vector observations were selected with values at the observation locations that were within ± 5 nT of the modeled lithospheric radial (B_r) and latitude (B_θ) components, and ± 3 nT of the modeled lithospheric longitude (B_ϕ) components.

Figure 2b shows the distributions of the airborne and selected CHAMP satellite residual data used for this study. These data were modeled by spherical harmonic Slepian functions up to degree 360 that required the evaluation of only 6104 coefficients. Global spherical harmonic modeling, by contrast, involves determining some 21 times this number of coefficients to represent



the spherical cap area shown in Fig. 2—i.e., with the core field components through degree 15 removed, the global spherical harmonic modeling required evaluating 130,065 ($=361^2 - 16^2$) coefficients.

Modeling multi-altitude data with spherical Slepian functions

This section describes the modeling of combined near-surface and satellite magnetic observations by spherical harmonic Slepian basis functions along with the relevant joint inversion procedures. Slepian functions (Slepian 1983) have been used for modeling noisy regional potential fields over an incomplete portion of the globe (Simons and Dahlen 2006), and to study gravity (e.g., Han and Simons 2008; Han 2008; Wang et al. 2012) and magnetic (e.g., Kim and von Frese 2013; Beggan et al. 2013; Plattner and Simons 2015) fields. However, the joint inversion of near-surface and satellite altitude magnetic observations relies on relatively standard least squares weighting procedures (e.g., Ravat et al. 2002; Menke 2012).

Following Simons and Dahlen (2006), a band-limited set of signals $f(\theta, \varphi)$ over the surface of a sphere can be represented by

$$f(\theta, \varphi) = \sum_{n=0}^N \sum_{m=-n}^n \gamma_{nm} Y_{nm}(\theta, \varphi) = \sum_{k=1}^{(N+1)^2} c_k S_k(\theta, \varphi), \quad (1)$$

using either conventional spherical harmonic functions $Y_{nm}(\theta, \varphi)$ with coefficients γ_{nm} of degree n and order m or Slepian basis functions $S_k(\theta, \varphi)$ with coefficients c_k , where N is the highest desired degree of the spherical harmonic expansion, and θ and φ are colatitude and longitude, respectively. Here, the k -th Slepian basis function is the linear combination of spherical harmonic functions with the corresponding coefficients $g_{k, nm}$ defined by

$$S_k(\theta, \varphi) = \sum_{n=0}^N \sum_{m=-n}^n g_{k, nm} Y_{nm}(\theta, \varphi). \quad (2)$$

For local modeling over the spherical cap of radius θ_0 , Slepian basis functions are required that maximize the ratio of energy concentrated within the spherical cap relative to the energy over the entire sphere given by

$$\lambda_k = \left(\int_0^{2\pi} \int_0^{\theta_0} S_k^2(\theta, \varphi) \sin \theta d\theta d\varphi \right) / \left(\int_0^{2\pi} \int_0^\pi S_k^2(\theta, \varphi) \sin \theta d\theta d\varphi \right). \quad (3)$$

Plugging $S_k(\theta, \varphi)$ from Eq. (2) into Eq. (3) and using the orthogonality properties of spherical harmonics converts Eq. (3) into the algebraic eigenvalue problem

$$\sum_{n=0}^N \sum_{m=-n}^n D_{nm, n' m'} g_{k, nm} = \lambda_k g_{k, n' m'} \quad (4)$$

with the localization kernel $D_{nm, n' m'} = \int_0^{2\pi} \int_0^{\theta_0} Y_{nm}(\theta, \varphi) Y_{n' m'}(\theta, \varphi) \sin \theta d\theta d\varphi$, for degrees n and n' and orders m and m' , where λ_k is the k -th eigenvalue and the associated eigenvector has the $(N+1)^2$ elements $g_{k, nm}$. Eigenvalues λ_k close to unity correspond to eigenvectors (or basis functions) that represent the features concentrated within the spherical cap, whereas the eigenvalues approaching null mark basis functions representing features outside the cap. Thus, the subset of Slepian basis functions corresponding to the higher eigenvalues from Eq. (4) optimally models the data concentrated over the spherical cap of interest.

In particular, for spherical harmonic degree N , the maximum number of basis functions or Shannon number (Simons and Dahlen 2006) is

$$K = \sum_{k=1}^{(N+1)^2} \lambda_k = \sum_{n=0}^N \sum_{m=-n}^n D_{nm, n' m'} = \frac{A}{4\pi} (N+1)^2, \quad (5)$$

for the spherical cap with area A relative to the surface area of the unit sphere (i.e., 4π). Thus, the Shannon number of basis functions to degree $N = 360$ is $K \approx 6104$ for the 25° -radius spherical cap centered on Australia in this study. The Slepian coefficients c_k in Eq. (1) for these basis functions are estimated by least squares from the spherical cap observations. In addition, the Slepian coefficients c_k are readily converted into the global spherical harmonic coefficients γ_{nm} up to degree N by combining Eqs. (1) and (2) to obtain

$$\gamma_{nm} = \sum_{k=1}^{(N+1)^2} c_k g_{k, nm}. \quad (6)$$

Because of the orthogonality properties of the eigenvectors, the Slepian coefficients may also be expressed in terms of the global spherical harmonic coefficients in Eq. (6) by

$$c_k = \sum_{n=0}^{(N+1)^2} \gamma_{nm} g_{k, nm} \quad (7)$$

The near-surface and satellite altitude data were combined into a Slepian spherical harmonic model by joint inversion (e.g., Ravat et al. 2002; Kim et al. 2004). In this study, Slepian spherical functions up to degree 360 that modeled 1° and longer-wavelength anomalies were established using the least squares matrix inversion problem given by

$$\mathbf{A} \mathbf{x} = \mathbf{b}. \quad (8)$$

Here, the design matrix \mathbf{A} holds the coefficients $S_k(\theta, \varphi)$ from Eqs. (1) and (2), whereas the solution column vector \mathbf{x} contains the unknown coefficients c_k in Eq. (1), and

the observation column vector \mathbf{b} holds the input magnetic anomaly data. For joint inversion, the design matrix is decomposed (Ravat et al. 2002; Kim et al. 2004) into submatrices \mathbf{A}_{ns} and \mathbf{A}_{sat} that reflect the Slepian expansions at the near-surface and satellite observation coordinates so that $\mathbf{A} = [\mathbf{A}_{\text{ns}} \ \mathbf{A}_{\text{sat}}]^T$. In addition, the observation vector is $\mathbf{b} = [\mathbf{b}_{\text{ns}} \ \mathbf{b}_{\text{sat}}]^T$ from the column vectors of the near-surface data \mathbf{b}_{ns} and satellite component observations \mathbf{b}_{sat} .

For the satellite magnetic vector observations, \mathbf{A}_{sat} is decomposed into $\mathbf{A}_{\text{sat}} = [\mathbf{A}_r^{\text{sat}} \ \mathbf{A}_\theta^{\text{sat}} \ \mathbf{A}_\phi^{\text{sat}}]^T$, where $\mathbf{A}_r^{\text{sat}}$, $\mathbf{A}_\theta^{\text{sat}}$, and $\mathbf{A}_\phi^{\text{sat}}$ are submatrices with Slepian expansions for each vector component. However, the near-surface total intensity anomalies for the study were assumed to be induced primarily by the main geomagnetic field to yield the $(23,472 \times 6104)$ matrix \mathbf{A}_{ns} . In general, the \mathbf{A}_{ns} elements also can be readily adapted to accommodate the superimposed vector effects of crustal magnetic remanence where known (e.g., Hinze et al. 2013). However, their incorporation was considered beyond the scope of the present study and thus ignored as these properties are relatively poorly assessed for the study region.

To obtain the joint solution of Slepian coefficients, the system in Eq. (8) was weighted to accommodate the different error budgets in the satellite and near-surface anomaly data (e.g., Ravat et al. 2002; Kim et al. 2004) using the weighted solution (e.g., Menke 2012) given by

$$\mathbf{x} = (\mathbf{A}^T \mathbf{W}_d \mathbf{A})^{-1} \mathbf{A}^T \mathbf{W}_d \mathbf{b}. \tag{9}$$

Here, the diagonal matrix \mathbf{W}_d holds weights given by the reciprocals of the input data variances, where $\sigma_{\text{sat}}^2 = (5.26^2, 4.31^2, 3.37^2) \text{ nT}^2$ for the respective radial, latitude, and longitude satellite vector component data, and $\sigma_{\text{ns}}^2 = 96.1^2 \text{ nT}^2$ for the near-surface data. The weighted solution was obtained using the minimum residual method (Paige and Saunders 1975) with a 0.001

solution tolerance and up to 57 iterations of the Matlab™ routine ‘*minres.m*’ (Matlab 2013).

Results

For this study, a total of 40,704 ($=13,568 \times 3$) CHAMP satellite vector observations and 23,472 near-surface total intensity data were used. The Australian near-surface low-pass filtered total intensity anomalies along with the distributions of the near-surface and CHAMP vector components within the 25°-radius study area are shown in Fig. 2a, b, respectively.

The performance of our regional degree 360 joint Slepian spherical harmonic model S360 is summarized in Table 1, where the strong correlation coefficients ($CC > 0.9$) show the Slepian model predictions are in good phase agreement with the near-surface and satellite data. In addition, the root-mean-squared (RMS) errors for the satellite B_r , B_θ , and B_ϕ components are about 1.5, 1.9, and 1.5 nT, respectively. For the near-surface total intensities (ΔT), the RMS error was about 38 nT and somewhat lower for the anomalies restricted to the Australian mainland and Tasmania with the oceanic areas excluded.

In general, near-surface magnetic anomaly predictions from joint modeling of satellite and near-surface anomalies (e.g., S360, NGDC720) are fundamentally ineffective for regions lacking near-surface observations due to the effects of data and modeling errors and the non-uniqueness of inversion (e.g., von Frese et al. 2005; Kim et al. 2013). Single-surface anomaly continuations are most reliable only over an altitude range corresponding to one or two station intervals of the data. Thus, the performance of the S360 model is optimally considered only over regions covered by both near-surface and satellite data—i.e., over the Australian mainland and Tasmania as shown in Fig. 3. In particular,

Table 1 Performance of the degree 360 Slepian joint satellite and near-surface magnetic anomaly model (S360)

Data	Input (nT)			S360 estimates (nT)			CC	RMS errors
	Max.; Min.	Avg.	Std.	Max.; Min.	Avg.	Std.		
CHAMP satellite vector components								
B_r	25.66; -19.23 (25.66; -17.51)	0.45 (1.56)	5.26 (5.96)	24.31; -20.74 (24.31; -18.74)	0.39 (1.44)	5.04 (5.77)	0.95 (0.98)	1.57 (1.28)
B_θ	23.03; -16.83 (12.98; -9.84)	0.79 (0.57)	4.31 (4.69)	22.18; -17.60 (16.89; -17.60)	0.17 (-0.17)	3.96 (4.41)	0.91 (0.94)	1.88 (1.77)
B_ϕ	12.98; -11.25 (12.98; -9.84)	0.23 (0.26)	3.37 (3.67)	11.29; -9.86 (10.97; -8.75)	0.12 (0.14)	2.99 (3.38)	0.90 (0.92)	1.47 (1.41)
Near-surface total intensities								
ΔT	749.8; -509.2 (749.8; -509.2)	-2.55 (7.82)	102.9 (116.1)	832.4; -455.0 (832.4; -455.0)	-1.99 (3.93)	95.8 (113.6)	0.93 (0.97)	38.1 (28.5)

Statistics include the amplitude maximum (Max.), minimum (Min.), average (Avg.), and standard deviation (Std.) values, and the related correlation coefficients (CC) and root-mean-squared (RMS) errors of the input and estimated anomaly data. The numbers in parentheses are for the Australian mainland and Tasmania

Fig. 3a illustrates the near-surface total intensity predictions from the S360 model, whereas Fig. 3b gives the differences from subtracting the predictions from the input anomalies with the performance statistics listed in Table 1.

The global spherical harmonic NGDC720 model is also based on the near-surface and satellite magnetic coverage of the study region (Maus 2010). Thus, as a further comparison, Fig. 3c shows the near-surface total intensity differences obtained by subtracting the NGDC720 predictions to degree 360 from the S360 model estimates with the statistics of this comparison listed at the

bottom of Table 2. In addition, Fig. 3d shows the differences between the input low-pass-filtered ΔT grid and the degree 360 predictions of NGDC720 with $CC = 0.82$ (or $= 0.94$ for just the Australian mainland and Tasmania) and $RMS\ error = 58.3$ (or $= 40.0$) nT. The north-south stripes in the two difference maps appear to reflect track-line noise from the along-track processing of the satellite orbital observations (e.g., Maus 2010; Kim et al. 1998).

At the mean 320 km altitude of CHAMP data, Fig. 4a–c shows the respective magnetic radial (B_r), latitude (B_θ), and longitude (B_ϕ) component anomaly estimates from

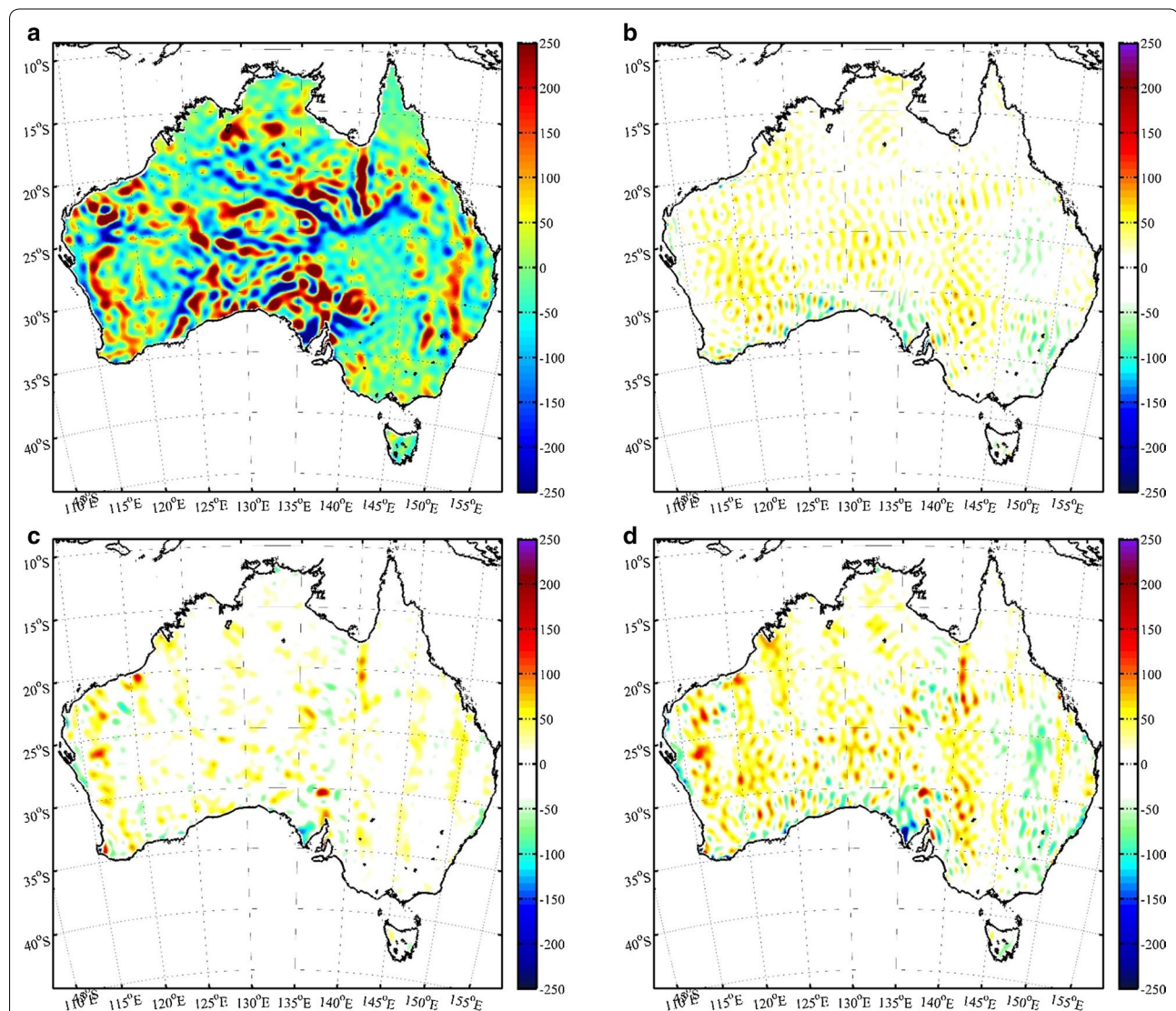


Fig. 3 **a** S360 model predictions of the near-surface total magnetic intensity anomalies for mainland Australia and Tasmania and **b** their differences; **c** commensurate near-surface total intensity anomaly differences between the S360 model and the degree 360 estimates of the NGDC720 model, and **d** the anomaly differences between the input near-surface low-pass-filtered total magnetic intensity anomaly grid and the degree 360 estimates of NGDC720. The statistics for these comparisons are listed in Tables 1 and 2

Table 2 Comparison of the degree 360 anomaly estimates (nT) from the S360 and NGDC720 models over the study area in Fig. 4

Components	S360 estimates			NGDC720 ($n \leq 360$) estimates			CC	RMS errors
	Max.; Min.	Avg.	Std.	Max.; Min.	Avg.	Std.		
Satellite altitude (320 km, $0.5^\circ \times 0.5^\circ$ grid)								
B_r	20.64; -16.05 (20.64; -15.82)	0.31 (1.39)	4.95 (5.82)	21.00; -17.29 (21.00; -17.29)	0.04 (0.99)	4.96 (5.93)	0.984 (0.996)	0.910 (0.665)
B_θ	15.94; -14.74 (14.21; -14.74)	0.02 (-0.17)	3.82 (4.43)	15.20; -15.08 (14.18; -15.08)	-0.10 (-0.45)	3.84 (4.47)	0.988 (0.998)	0.647 (0.388)
B_ϕ	9.77; -7.56 (9.77; -7.41)	0.09 (0.18)	2.91 (3.40)	9.98; -8.58 (9.98; -7.03)	-0.03 (0.06)	2.97 (3.41)	0.974 (0.990)	0.685 (0.510)
Near surface ($0.25^\circ \times 0.25^\circ$)								
ΔT	832.4; -455.0 (832.4; -455.0)	-1.99 (3.93)	95.8 (113.6)	871.8; -438.7 (765.5; -438.7)	-0.52 (4.08)	83.45 (101.3)	0.89 (0.97)	44.2 (27.7)

See Table 1 for the abbreviations of the listed statistics. The numbers in parentheses are for the Australian mainland and Tasmania

Table 3 Anomaly statistics for Figs. 1, 2, 3, 4, 6, and 7 to facilitate reproducing the maps

Maps	Magnetic anomalies (nT)			Figure no.	Magnetic anomalies (nT)				
	Max.; Min.	Avg.	Std.		Max.; Min.	Avg.	Std.		
Figure 1	a	28,665; -10,997	3.71	263	Figure 6	c	(288; -121)	(3.6)	(44.5)
Figure 2	a	750; -509	-2.55	102		d	(177; -81.7)	(3.4)	(31.9)
Figure 3	a	832.4; -455.0 (832.4; -455.0)	-1.99 (3.93)	95.8 (113.6)		e	(113; -63.5)	(3.2)	(24.5)
	b	400; -351 (121; -224)	-1.0 (3.7)	38.0 (28.3)		f	(59.3; -42.0)	(2.6)	(16.1)
	c	400; -351 (176; -318)	-1.0 (-0.0)	38.0 (27.8)		g	(41.5; -30.0)	(2.1)	(11.5)
	d	543; -664 (195; -366)	-2.0 (3.7)	58.2 (40.0)		h	(26.5; -19.8)	(1.7)	(7.4)
Figure 4 ^a	d	4.03; -4.14 (1.81; -1.64)	0.26 (0.40)	0.87 (0.53)	Figure 7	a	(304; -181)	(3.7)	(59.6)
	e	3.42; -3.16 (1.27; -0.70)	0.29 (0.28)	0.58 (0.27)		b	(671; -373)	(10.0)	(101)
	f	5.10; -3.40 (1.23; -1.55)	0.12 (0.13)	0.67 (0.49)		c	(489; -448)	(-6.4)	(81.7)
						d	(25.9; -20.3)	(1.2)	(7.6)
Figure 6	a	(687; -362)	(3.7)	(99.6)		e	(30.5; -17.5)	(5.2)	(8.5)
	b	(489; -222)	(3.8)	(70.0)		f	(15.0; -23.5)	(-4.0)	(6.2)

See Table 1 for the abbreviations of the listed statistics. The numbers in parentheses are for the Australian mainland and Tasmania

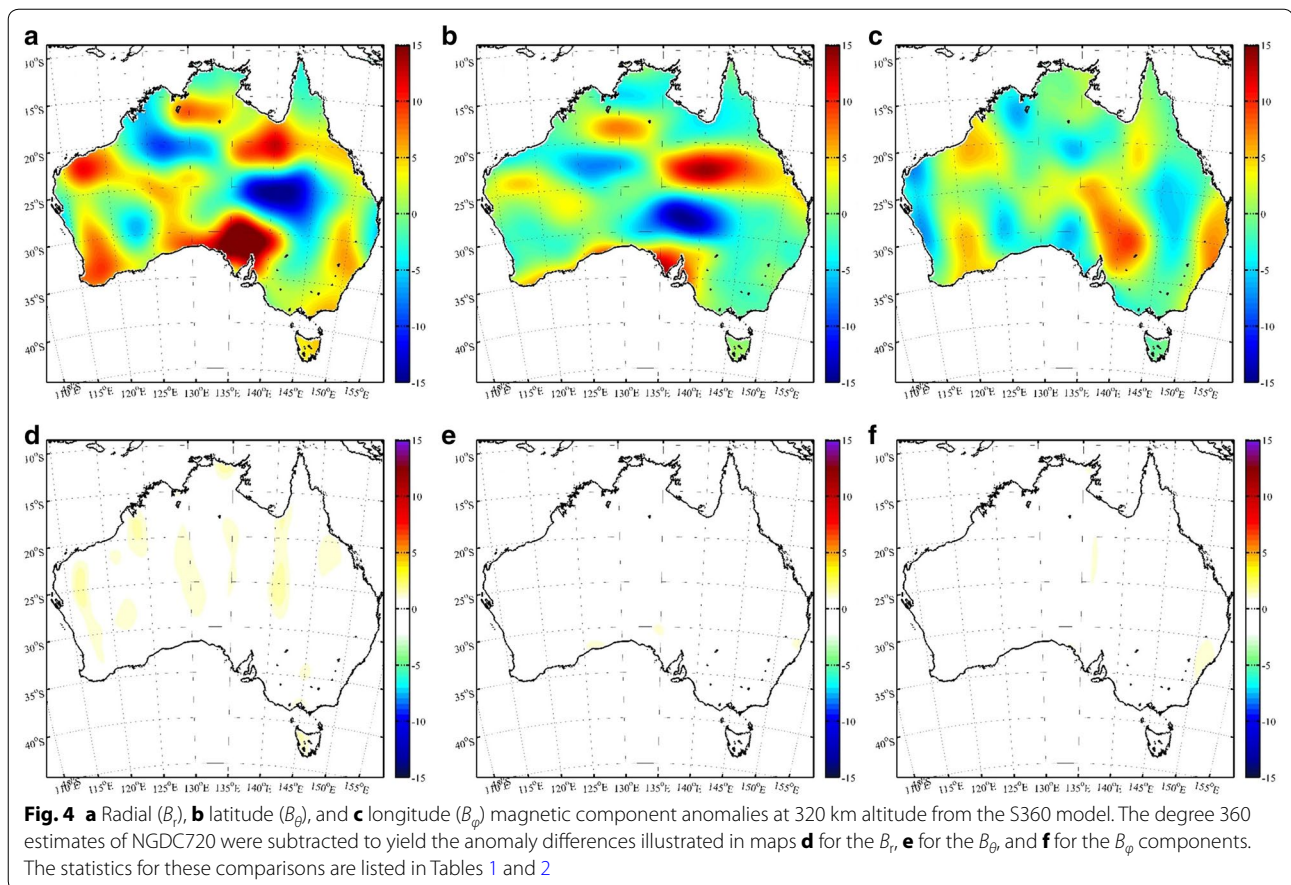
^a The S360 model statistics of maps a, b, and c are listed in Table 2

the S360 model. The corresponding differences relative to the degree 360 estimates of the global NGDC720 model are relatively minor as illustrated in Fig. 4d–f, respectively, with the affiliated statistics listed in Table 2.

Discussion

Figure 5a compares the Lowes–Mauersberger power spectra (Lowes 1974) of the S360 and NGDC720 models. Here, the spectrum for the S360 model (*blue* x's) up to degree 360 involves the global spherical harmonic

coefficients from Eq. (6) conversion of the Slepian coefficients obtained by the weighted least squares solution in Eq. (9). The band-limited ($16 \leq n \leq 360$) spectrum based on the spherical harmonic coefficients of the global NGDC720 model (black circles) reflects essentially lithospheric components minus the core field components up to degree 15. The power spectrum of the localized NGDC720 model (red crosses) up to degree 360 is based on a set of localized spherical harmonic coefficients obtained via Eq. (6) from localized Slepian coefficients



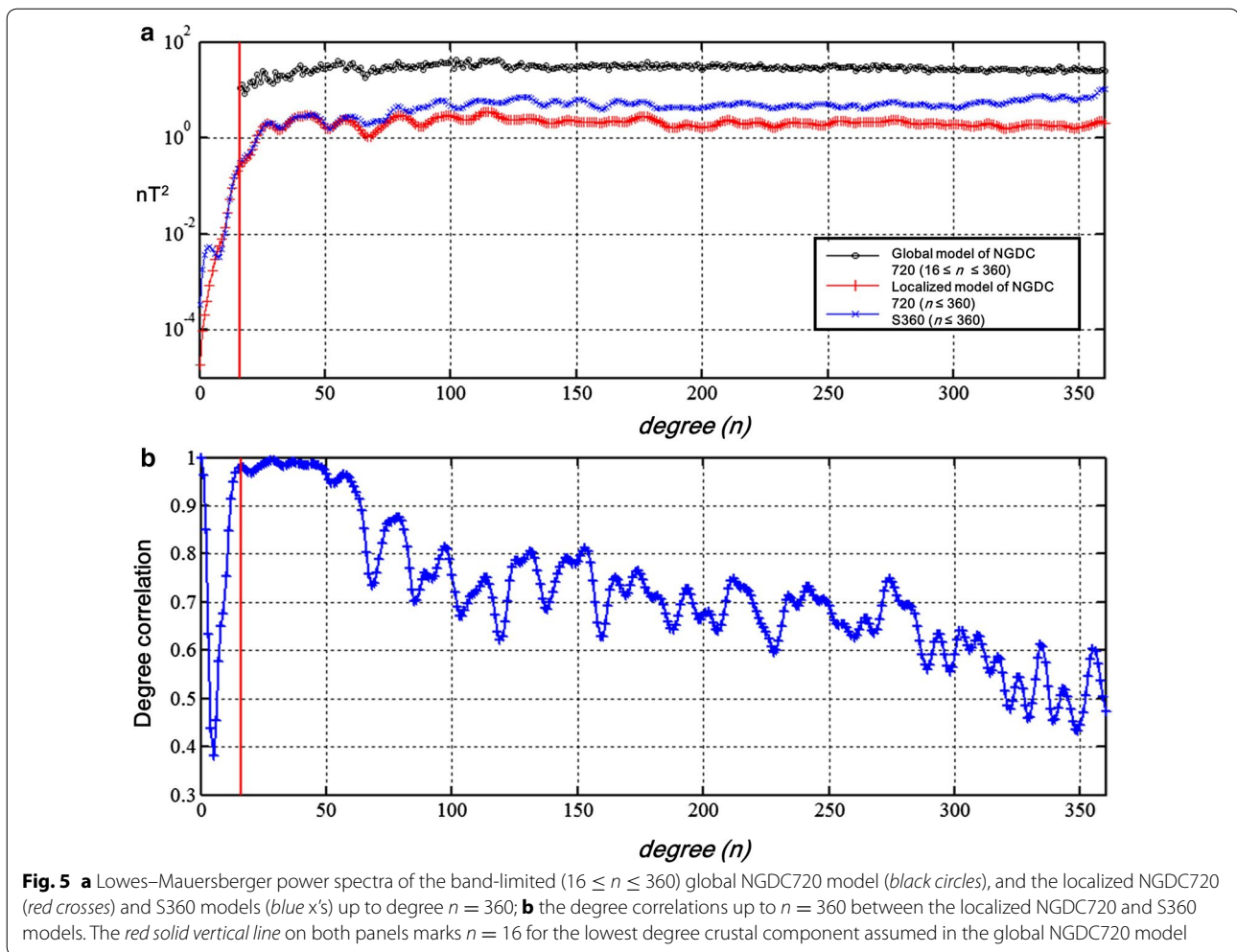
that were developed by Eq. (7) from the global set of spherical harmonics.

The degree correlation curve (e.g., Langel and Hinze 1998) in Fig. 5b suggests that the highly correlated behavior of the two localized models between degrees 16 through 60 breaks down at higher orders. Thus, the differences between the longer-wavelength localized NGDC720 and S360 anomaly estimates are relatively minimal at the satellite altitude. However, at the higher degrees, the S360 predictions have greater lithospheric anomaly power than the localized NGDC720 model because the energy level (i.e., standard deviation) of the near-surface grids used for producing the S360 model is greater than that of the localized near-surface NGDC720 model predictions. The band-limited global NGDC720 model yields the spectrum with greatest power because the global mean power value is greater than the mean anomaly power within the Australian cap.

Figure 6 provides perspectives on how the radial crustal magnetic anomaly components for Australia may vary over altitudes ranging from 10 to 275 km. For example, the large negative magnetic anomaly at 275 km altitude overlying the Simpson Desert (Sd) between the

North Australian Craton (NAC in Fig. 1b) and the Central Mobile Belts (CMB in Fig. 1b) becomes increasingly broken up at around 150 km and lower altitudes. The anomaly break up may reflect the presence of the positive magnetic effects of a thickened Proterozoic Musgrave Orogen crustal block (Mu) that seismic Moho depth estimates (Salmon et al. 2013) suggest connected the thickened crust of the West Australian Craton (WAC). Additional anomaly features that may reflect crustal thickness variations include the positive anomalies overlying the Mt. Isa (Ms) inlier in the seismically estimated 50-km-thick crust of the North Australian Craton (NAC in Fig. 1b) and the Adelaide block (Ad) in the 70-km-thick crust of the South Australian Craton. At lower altitudes, both anomaly features describe strong, complicated short-wavelength features and constraints on the underlying tectonic features.

Additional examples include the strong Adelaide anomaly (Ad), which may have been part of a prominent positive anomaly overlying a putative meteorite impact basin in Wilkes Land, Antarctica that became detached in the Cretaceous separation of Australia from East Antarctica (von Frese et al. 2013). Indeed, the effects of partial



impact ring structures in the Adelaide crust become perceptible in Fig. 6 at altitudes of about 75 km and lower. At the higher altitudes, the modeled magnetic anomalies are largely consistent with regional crustal thickness estimates from magnetic (Chopping and Kennett 2015) and seismic (Salmon et al. 2013) studies. In addition, the major negative anomalies overlying the Great Sandy Desert (Gs) in the west and the Simpson Desert (Sd) in the east at 275 km altitude correspond well with gravity-inferred reduced Moho depths (e.g., Aitken 2010; Aitken et al. 2013; Salmon et al. 2013).

In general, the S360 model facilitates extending to satellite altitude the numerous near-surface anomaly interpretations developed since the compilation's completion (e.g., Milligan et al. 2003). However, like the results of any potential field inversion, the S360 model estimates are not unique and subject to measurement and modeling errors (e.g., von Frese et al. 2005; Kim et al. 2013), which make them fundamentally unreliable where measurements are lacking such as in the large near-surface survey

coverage gaps. In principle, the effectiveness of the localized S360 model can only be improved by mapping new data within the near-surface coverage gaps and at intermediate altitudes.

The altitude perspectives on the anomalies in Fig. 6 are consistent with the boundary values imposed by both the near-surface and satellite observations. That is, they cannot be derived simply from upward continuing only the near-surface anomalies or downward continuing just the satellite anomalies because of the observational and data processing errors and the non-uniqueness of anomaly continuation (e.g., von Frese et al. 2005; Kim et al. 2013).

To help illustrate the limitations in these single-surface continuations, consider the correlative properties between the satellite and near-surface anomaly continuations at 10 km altitude highlighted in Fig. 7a, b, respectively, with the differences (7a – 7b) shown in Fig. 7c. The affiliated correlation coefficient CC (7a, 7b) = 0.58 suggests that the downward continued CHAMP data have recovered only about 34% of the upward continued

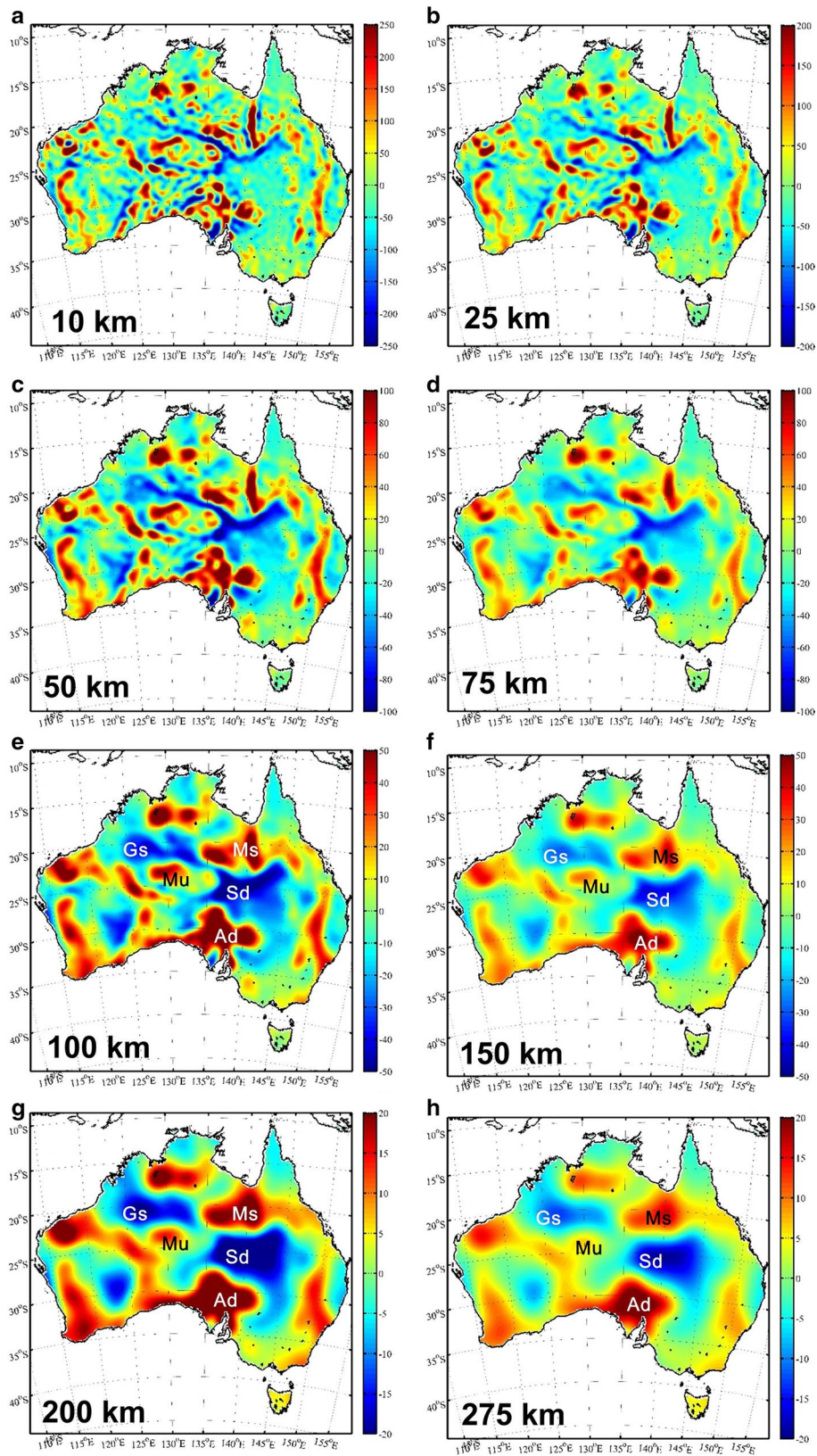


Fig. 6 Radial component magnetic anomalies of Australia estimated from the 5360 model over the altitudes **a** at 10 km, **b** at 25 km, **c** at 50 km, **d** at 75 km, **e** at 100 km, **f** at 150 km, **g** at 200 km and **h** at 275 km, respectively. The feature annotations are listed in Fig 1b

near-surface anomalies at the 10-km altitude. On the other hand, Fig. 7b correlates with the S360 predictions in Fig. 6a from the joint inversion of satellite and near-surface anomalies at CC (7b, 6a) = 0.98 to suggest an improvement of some 185% in the recovery of the 10-km-altitude anomalies.

The maps in Fig. 7d, e, on the other hand, show the respective CHAMP and near-surface anomaly continuations at 275 km altitude with map 7f giving the differences (7e – 7d). Here, the CC (7d, 7e) = 0.70 correlation infers the recovery of only about 49% of the CHAMP anomalies by the upward continued near-surface data, whereas the CC (7d, 6h) = 0.99 correlation suggests a nearly 100% improvement in recovering the satellite altitude anomalies with the S360 model predictions (Fig. 6h).

In general, the computational efficiency suggested by the Slepian coefficient model of Australia's near-surface and satellite altitude magnetic anomaly data clearly can be significant for other multi-altitude compilations such as the next-generation magnetic anomaly map (ADMAPP-2) that the Antarctic Digital Magnetic Anomaly Project is compiling for the Antarctic south of 60°S (e.g., Golynsky et al. 2001; von Frese et al. 2008). The Slepian coefficients

may be rendered as a localized regional model (e.g., S360) or integrated into a global model (e.g., NGDC720) to estimate effective magnetic anomaly scalar, vector, and gradient components at all spherical coordinates on and between the mapped observation surfaces. However, anomaly continuations over increasing distances above and below the bounding observation surfaces are increasingly limited due to data and modeling errors and the inherent non-uniqueness of continuation.

Conclusions

This study demonstrated the utility of localized Slepian basis functions to model near-surface low-pass-filtered total intensity and selected CHAMP satellite vector magnetic anomalies over a 25°-radius cap centered on Australia. Effective Slepian spherical harmonic coefficients were obtained by weighted least squares inversion of the multi-altitude data sets. Relative to global spherical harmonic models, far fewer Slepian spherical harmonic coefficients are needed for honoring the smaller wavelength properties of the localized observations. However, the Slepian coefficients also can be used to update the global spherical harmonic coefficients, and thus, Slepian

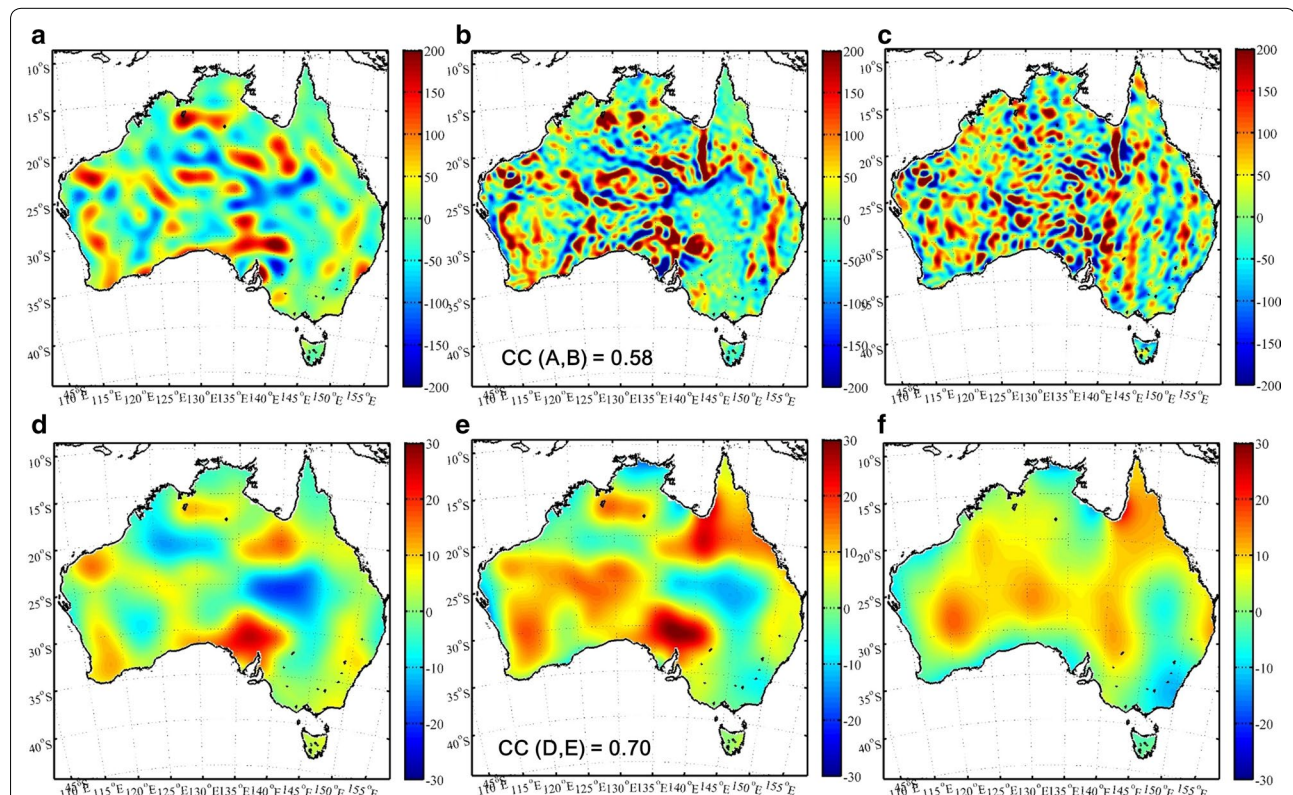


Fig. 7 Maps **a** and **b** compare at 10 km altitude the respective downward continued CHAMP (i.e., MF7 model from Maus 2010) and upward continued near-surface anomalies with the anomaly differences (Map **a** – Map **b**) shown in Map **c**, whereas Maps **d** and **e** contrast at 275 km altitude the respective downward continued CHAMP and upward continued near-surface anomalies with the anomaly differences (Map **d** – Map **e**) given in Map **f**. Included on maps **b** and **e** are the respective correlation coefficients between maps **a** and **b**, and maps **e** and **d**

modeling can be efficient for updating global spherical harmonic models with new data. This approach will be particularly effective for updating global spherical harmonic models for new satellite observations such as from the Swarm mission (e.g., Thébaud et al. 2016; Olsen et al. 2016) and new aeromagnetic surveys such as in the Antarctic (e.g., Kim et al. 2013; Golynsky et al. 2013; von Frese et al. 2008), the oceans, and other large unsurveyed regions of the Earth.

The localized Slepian model (S360) fully honors both near-surface and satellite input data for improved perspectives on how the magnetic anomalies of the lithosphere may vary over the intervening altitudes. These perspectives are not available from standard downward or upward continuations of the individual data sets. However, these continuations represent inversion results that are not unique and subject to measurement and modeling errors so that their interpretation at locations lacking magnetic observations requires considerable care.

Authors' contributions

HRK led the study and carried out its data processing, modeling and graphical efforts. RvF contributed discussion and interpretation elements. Both authors read and approved the final manuscript.

Author details

¹ Department of GeoEnvironmental Science, Kongju National University, Gongju, Chungnam, South Korea. ² School of Earth Sciences, The Ohio State University, Columbus, OH, USA.

Acknowledgements

This work was supported by a 2013 research grant from Kongju National University. The CHAMP data in this study are publicly available from the Technical University of Denmark website (www.space.dtu.dk). The S360 model is available from HRK upon e-mail request. This work also benefitted from the constructive comments and recommendations of two anonymous reviewers.

Competing interests

The authors declare that they have no competing interests.

Publisher's Note

Springer Nature remains neutral with regard to jurisdictional claims in published maps and institutional affiliations.

Received: 10 November 2016 Accepted: 6 April 2017

Published online: 18 April 2017

References

- Aitken AR (2010) Moho geometry gravity inversion experiment (MoGGIE): a refined model of the Australian Moho, and its tectonic and isostatic implications. *Earth Planet Sci Lett* 297(1):71–83
- Aitken AR, Salmon M, Kennett B (2013) Australia's Moho: a test of the usefulness of gravity modelling for the determination of Moho depth. *Tectonophysics* 609:468–479
- Beggan CD, Saarimaki J, Whaler KA, Simons FJ (2013) Spectral and spatial decomposition of lithospheric magnetic field models using spherical Slepian functions. *Geophys J Int* 193:136–148
- Blake DH, Kilgour B (1998) Geological Regions (National Geoscience Dataset), 1:5 million scale digital map dataset. Geoscience Australia, Canberra
- Blakely RJ (1995) Potential theory in gravity and magnetic applications. Cambridge University Press, New York
- Chopping R, Kennett BL (2015) Maximum depth of magnetisation of Australia, its uncertainty, and implications for Curie depth. *GeoResJ* 7:70–77
- Coles RL (1985) Magsat scalar magnetic anomalies at northern high latitudes. *J Geophys Res* 90(B3):2576–2582
- de Santis A, Kerridge DJ, Barraclough DR (1989) A spherical cap harmonic model of the crustal magnetic anomaly field in Europe by Magsat. In Lowes FJ et al (eds) *Geomagnetism and paleomagnetism*. pp 1–17
- Gaya-Piqué LR, Ravat D, De Santis A, Torta JM (2006) New model alternatives for improving the representation of the core magnetic field of Antarctica. *Antarct Sci* 18(01):101–109
- Golynsky A, Chiappini M, Damaske D, Ferraccioli F, Ferris J, Finn C, Ghidella M, Ishihara T, Johnson A, Kim HR, Kovács L, LaBrecque J, Masolov V, Nogi Y, Purucker M, Taylor P, Torta M (2001) ADMAP—magnetic anomaly map of the Antarctic, 1:10 000 000 scale map. BAS (Misc.) 10. British Antarctic Survey, Cambridge
- Golynsky A, Bell R, Blankenship D, Damaske D, Ferraccioli F, Finn C et al (2013) Air and shipborne magnetic surveys of the Antarctic into the 21st century. *Tectonophysics* 585:3–12
- Haines GV (1985) Spherical cap harmonic analysis. *J Geophys Res* 90(B3):2583–2591
- Haines GV (1990) Regional magnetic field modelling: a review. *J Geomagn Geoelectr* 42:1001–1101
- Han S-C (2008) Improved regional gravity fields on the Moon from Lunar Prospector tracking data by means of localized spherical harmonic functions. *J Geophys Res* 113:E11012. doi:10.1029/2008JE003166
- Han S-C, Simons FJ (2008) Spatiospectral localization of global geopotential fields from the Gravity Recovery and Climate Experiment (GRACE) reveals the coseismic gravity change owing to the 2004 Sumatra–Andaman earthquake. *J Geophys Res* 113:B01405. doi:10.1029/2007JB004927
- Hildenbrand TG, Blakely R, Hinze WJ, Keller R, Langel RA, Nabighian M, Roest W (1996) Aeromagnetic survey over U.S. to advance geomagnetic research. *Eos* 77:265
- Hinze WJ, von Frese RRB, Saad AH (2013) Gravity and magnetic exploration: principles, practices, and applications. Cambridge University Press, Cambridge
- Kim HR, von Frese RRB (2013) Localized analysis of polar geomagnetic jerks. *Tectonophysics* 585:26–33
- Kim JW, Kim J, von Frese RRB, Roman DR, Jezek K (1998) Spectral attenuation of track-line noise. *Geophys Res Lett* 25:187–190
- Kim HR, von Frese RRB, Golynsky AV, Taylor PT, Kim JW (2004) Application of satellite magnetic observations for estimating near-surface magnetic anomalies. *Earth Planets Space* 56(10):955–966. doi:10.1186/BF03351793
- Kim HR, von Frese RRB, Golynsky AV, Taylor PT, Kim JW (2005) Crustal analysis of Maud Rise from combined satellite and near-surface magnetic survey data. *Earth Planets Space* 57(8):717–726. doi:10.1186/bf03351851
- Kim HR, von Frese RRB, Golynsky AV, Taylor PT, Gaya-Piqué LR, Ferraccioli F (2007) Improved magnetic anomalies of the Antarctic lithosphere from satellite and near-surface data. *Geophys J Int* 171:119–126
- Kim HR, von Frese RRB, Hong JK, Golynsky AV (2013) A regional lithospheric magnetic modeling over Antarctic region. *EGU Gen Assem Conf Abstr* 15:5491
- Kotzé PB (2001) Spherical cap modelling of Ørsted magnetic field vectors over southern Africa. *Earth Planets Space* 53(5):357–361. doi:10.1186/BF03352392
- Kovács P, Vujic E, Csontos A, Brkic M, Heilig B, Koppán A (2011) Regional magnetic field model for Croatia and Hungary. In: 6th congress of the Balkan Geophysical Society
- Langel RA, Hinze WJ (1998) The magnetic field of the Earth's lithosphere. Cambridge
- Lesur V (2006) Introducing localized constraints in global geomagnetic field modelling. *Earth Planets Space* 58(4):477–483. doi:10.1186/BF03351943
- Lowes FJ (1974) Spatial power spectrum of the main geomagnetic field, and extrapolation to the core. *Geophys J Int* 36(3):717–730
- MATLAB (2013) Release 2013b. The MathWorks Inc, Natick
- Maus S (2010) An ellipsoidal harmonic representation of Earth's lithospheric magnetic field to degree and order 720. *Geochem Geophys Geosyst* 11(6):Q06015. doi:10.1029/2010GC003026
- Maus S, Barckhausen U, Berkenbosch H, Bournas N, Brozina J, Childers V, Dostaler F, Fairhead JD, Finn C, von Frese RRB et al (2009) EMAG2: a 2-arc min resolution Earth Magnetic Anomaly Grid compiled from satellite, airborne, and marine magnetic measurements. *Geochem Geophys Geosyst* 10:Q08005. doi:10.1029/2009GC002471

- Menke W (2012) *Geophysical data analysis: discrete inverse theory*. Academic Press, New York
- Milligan PR, Franklin R (2004) *Magnetic anomaly map of Australia (Fourth Ed.)*, 1:5,000,000 scale. Geoscience Australia, Canberra
- Milligan PR, Petkovic P, Drummond BJ (2003) Potential field datasets for the Australian region: their significance in mapping basement architecture. *Geol Soc Aust Spec Publ* 22:123–133
- Milligan PR, Franklin R, Ravat D (2004) A new generation of Magnetic Anomaly Grid Database of Australia (MAGDA)—use of independent data increases the accuracy of long wavelength components of continental-scale merges. *Preview* 113:25–29
- Milligan PR, Franklin R, Minty BRS, Richardson LM, Percival PJ (2010) *Magnetic anomaly map of Australia (Fifth Edition)*, 1:5,000,000 scale. Geoscience Australia, Canberra
- Olsen N, Lühr H, Finlay CC, Sabaka TJ, Michaelis I, Rauberg J, Tøffner-Clausen L (2014) The CHAOS-4 geomagnetic field model. *Geophys J Int* 197(2):815–827
- Olsen N, Finlay CC, Kotsiaros S, Clausen LT (2016) A model of Earth's magnetic field derived from 2 years of Swarm satellite constellation data. *Earth Planets Space* 68(1):124. doi:10.1186/s40623-016-0488-z
- Paige CC, Saunders MA (1975) Solution of sparse indefinite systems of linear equations. *SIAM J Numer Anal* 12:617–629
- Plattner A, Simons FJ (2015) High-resolution local magnetic field models for the Martian South Pole from Mars Global Surveyor data. *J Geophys Res* 120:1543–1566
- Ravat D, Whaler KA, Pilkington M, Sabaka T, Purucker M (2002) Compatibility of high-altitude aeromagnetic and satellite-altitude magnetic anomalies over Canada. *Geophysics* 67(2):546–554
- Salmon M, Kennett B, Stern T, Aitken A (2013) The Moho in Australia and New Zealand. *Tectonophysics* 609:288–298
- Simons FJ, Dahlen FA (2006) Spherical Slepian functions and the polar gap in geodesy. *Geophys J Int* 166(3):1039–1061
- Slepian D (1983) Some comments on Fourier analysis, uncertainty and modeling. *SIAM Rev* 25(3):379–393
- Thébault E, Schott JJ, Manda M (2006) Revised spherical cap harmonic analysis (R-SCHA): validation and properties. *J Geophys Res* 111:B01102. doi:10.1029/2005JB003836
- Thébault E, Vigneron P, Langlais B, Hulot G (2016) A Swarm lithospheric magnetic field model to SH degree 80. *Earth Planets Space* 68(1):126. doi:10.1186/s40623-016-0510-5
- von Frese RRB (1998) Correction to: von Frese, R.R.B., W.J. Hinze, and L.W. Braille, Spherical earth gravity and magnetic anomaly analysis by equivalent source inversion (*Earth Planet. Sci. Lett.*, 53, 69–83, 1981). *Earth Planet Sci Lett* 163:409–411
- von Frese RRB, Hinze WJ, Braille LW (1981) Spherical earth gravity and magnetic anomaly analysis by equivalent point source inversion. *Earth Planet Sci Lett* 53:69–83
- von Frese RRB, Ravat DN, Hinze WJ, McGue CA (1988) Improved inversion of geopotential field anomalies for lithospheric investigations. *Geophysics* 53:375–385
- von Frese RRB, Kim HR, Tan L, Kim JW, Taylor PT, Purucker M, Alsdorf D, Raymond CA (1999) Satellite magnetic anomalies of the Antarctic crust. *Ann di Geofis* 42:309–326
- von Frese RRB, Kim HR, Taylor PT, Asgharzadeh MF (2005) Reliability of CHAMP anomaly continuations. In: Reigber C (ed) *Earth observation with CHAMP*. Springer, Berlin, pp 287–292
- von Frese RRB, Golynsky AV, Kim HR, Gaya-Piqué L, Thébault E, Chiappini M, Ghidella M, Grunow A, The ADMAP Working Group (2008) The next generation Antarctic digital magnetic anomaly map. In: Cooper AK, Raymond CA (eds) *Proceedings of the 10th ISAES, USGS open-file rept.* 2007-1047. doi:10.3133/of2007.srp163
- von Frese RRB, Kim HR, Leftwich TE, Kim JW, Golynsky AV (2013) Satellite magnetic anomalies of the Antarctic Wilkes Land impact basin inferred from regional gravity and terrain data. *Tectonophysics* 585:185–195
- Wang L, Shum CK, Simons FJ, Tapley B, Dai CL (2012) Coseismic and post-seismic deformation of the 2011 Tohoku-Oki earthquake constrained by GRACE gravimetry. *Geophys Res Lett* 39:L07301. doi:10.1029/2012GL051110

Submit your manuscript to a SpringerOpen® journal and benefit from:

- Convenient online submission
- Rigorous peer review
- Immediate publication on acceptance
- Open access: articles freely available online
- High visibility within the field
- Retaining the copyright to your article

Submit your next manuscript at ► springeropen.com
